WILEY-VCH

DOI: 10.1002/18
Article type: Full paper

Twin Engineering in Solution-Synthesized Non-stoichiometric Cu_5FeS_4 Icosahedral Nanoparticles for Enhanced Thermoelectric Performance

*Aijuan Zhang,[1] Bin Zhang,[4] Wei Lu,[5] Dandan Xie,[1] Hongxia Ou,[1] Xiaodong Han,[4] Jiyan Dai,[5] Xu Lu,[1] Guang Han,[*2] Guoyu Wang,[*3] and Xiaoyuan Zhou[*1]*

[a] A. Zhang, D. Xie, H. Ou, Prof. X. Lu, Prof. X. Zhou
College of Physics, Chongqing University, Chongqing 401331, China
E-mail: xiaoyuan2013@cqu.edu.cn
[b] Prof. G. Han
College of Materials Science and Engineering, Chongqing University, Chongqing 400044, China
E-mail: guang.han@cqu.edu.cn
[c] Prof. G. Wang
Chongqing Institute of Green and Intelligent Technology, Chinese Academy of Sciences, Chongqing 400714, China
E-mail: guoyuw@cigit.ac.cn
[d] Dr. B. Zhang, Prof. X. Han
Beijing Key Lab of Microstructure and Property of Advanced Materials, Beijing University of Technology, Beijing, 100024, China
[e] Dr. W. Lu, Prof. J. Dai
Department of Applied Physics, The Hong Kong Polytechnic University, Kowloon, Hong Kong

A.Z. and B.Z. contributed equally to this work.

Keywords: Cu_5FeS_4, twin engineering, thermoelectric, non-stoichiometry, nanomaterial

Abstract: A facile colloidal solution method has been developed for the fast, scalable synthesis of orthorhombic@cubic core-shell non-stoichiometric Cu_5FeS_4 icosahedral nanoparticles. Such nanoparticles contain high-density twin boundaries in the form of five-fold twins. Spark plasma sintering consolidates the nanoparticles into nanostructured pellets, which retain high-density twin boundaries and a tuned fraction of the secondary phase Fe-deficient cubic Cu_5FeS_4. As a result, the thermal and electrical transport properties are synergistically optimized, leading to an enhanced zT of ~0.62 at 710 K, which is about 51% higher than that of single-phase Cu_5FeS_4. This study provides an energy-efficient approach to realize twin engineering in non-stoichiometric Cu_5FeS_4 nanomaterials for high-performance thermoelectrics.

1. Introduction

Declining fossil fuel reserves, together with ever-growing global energy demands, have stimulated the world-wide interests in high performing energy conversion technologies.[1-2] Thermoelectrics, capable of directly converting thermal energy into electric energy, can be utilized to generate useful electricity from waste heat, thus possessing potential in alleviating the energy demands. The conversion efficiency of a thermoelectric material is determined by its dimensionless figure of merit (zT), $zT = S^2\sigma T/\kappa$, where S, σ, T and κ denote respectively the Seebeck coefficient, electrical conductivity, absolute temperature and thermal conductivity.[3-8] Recently, Cu-based sulfides have attracted extensive attention as potentially useful thermoelectric materials, due to their competitive zT coupled with low toxicity and cost.[9-16] One of the promising candidates is Cu_5FeS_4 (also known as bornite) that exhibits complex cation order-disorder phase transitions upon heating, transforming from the orthorhombic phase (*Pbca*, $a = c \sim 10.95$ Å, $b \sim 21.86$ Å) through the intermediate cubic phase ($Fm\bar{3}m$, $a \sim 10.95$ Å) to the high cubic phase ($Fm\bar{3}m$, $a \sim 5.49$ Å), when heated from 300 K through 473 K to 543 K.[12] The high cubic phase possesses completely disordered distribution of Cu, Fe and vacancies in the centers of S tetrahedrons, which largely disturbs phonon transport and results in low lattice thermal conductivity.[12] To improve electrical conductivity, non-stoichiometric bornite with more Cu and less Fe was synthesized, which demonstrated higher carrier concentration and an enhanced zT of ~0.52 at 700 K.[12] Nevertheless, Cu_5FeS_4 has been primarily fabricated via high-temperature, energy-intensive method. Alternative low-cost, scalable solution synthesis has also been exploited to synthesize high-performance non-stoichiometric bornite (zT ~0.56, 690 K).[17]

Defect engineering[18-20] has proven effective to optimize the thermal[21-27] and electronic[28-35] properties of a diversity of thermoelectric materials. Defects, such as point defects, dislocations and grain boundaries, can enhance scattering of phonons with varied mean free paths, reducing the lattice thermal conductivity (κ_L).[21-26] Twin boundaries are expected to

decrease κ_L through enhanced phonon scattering, while exert minor influence on carrier mobility due to their ordered atomic arrangement.[36,37] These boundaries could also scatter low-energy carriers to improve the Seebeck coefficient, as demonstrated in twin-containing $Bi_{0.5}Sb_{1.5}Te_3$.[36] Therefore, twin engineering provides a potential strategy to synergistically optimize the thermal and electrical transport properties. Few attempts combined melting spinning, ball milling and spark plasma sintering (or hot pressing) to introduce twin boundaries into bulk materials (e.g. Bi_2Te_3, Cu-Ni alloy)[36,37] yet without control on their density and never realized in Cu-based sulfide (e.g. Cu_5FeS_4). Although inexpensive solution synthesis is capable of controlling grain sizes in thermoelectric nanomaterials (and therefore grain boundaries in sintered compacts),[38-42] controlling the formation and density of twin boundaries proves challenging. Hence, it is pivotal to develop a new strategy to realize the formation and control the density of twin boundaries in thermoelectric compounds.

Icosahedral nanocrystal represents a fascinating polyhedral structure that typically consists of 20 tetrahedral sub-units separated by 30 twin boundaries and has a surface enclosed by 20 {111} crystal facets (for a cubic crystal structure).[43] Synthesizing such icosahedral nanocrystals provides a potential controllable approach to introduce high-density twin boundaries into thermoelectric materials. However, the synthesis of icosahedral nanocrystals is primarily realized in cubic-structured metals and never in Cu_5FeS_4.[43,44] Herein, we demonstrate the controllable solution synthesis of Cu_5FeS_4 icosahedral nanoparticles containing high-density twin boundaries through a fast, scalable colloidal synthesis method. Further, in order to tune the carrier concentration, we selectively grow Fe-deficient cubic Cu_5FeS_4 as the nanoparticle shell, leading to the formation of orthorhombic@cubic core-shell structures. The icosahedral core-shell nanoparticles can be sintered into nanostructured compacts retaining high density of twin boundaries and a tuned fraction of the cubic Cu_5FeS_4, leading to the synergistic optimization of electrical and thermal transport properties.

2. Results and discussion

2.1 Characterization of Cu_5FeS_4 icosahedral nanoparticles

The solution synthesis of Cu_5FeS_4 icosahedral nanoparticles requires well-controlled experimental parameters, involving heating a mixture of a S-oleylamine (OLA) solution and a $CuCl_2$-$Fe(acac)_3$-OLA solution at 553 K for 30 min (see Experimental Details; Figure S1). Powder X-ray diffraction (PXRD) patterns (**Figure 1a**) can be indexed to mixed phases of orthorhombic Cu_5FeS_4 (denoted as orth-Cu_5FeS_4; PDF card No. 42-0586) with lattice parameters $a = c$ of *ca.* 10.96 Å and b of *ca.* 21.81 Å and cubic Cu_5FeS_4 (denoted as cubic-Cu_5FeS_4; PDF card No. 24-0050) with a of *ca.* 5.52 Å. The relation between their lattice parameters, that is, a(cubic-Cu_5FeS_4) is approximately 1/2 of a(orth-Cu_5FeS_4) and 1/4 of b(orth-Cu_5FeS_4), leads to the appearance of several "double peaks" in the PXRD patterns, e.g. 111, 200, 220 peaks of cubic-Cu_5FeS_4 are next to 242, 080 and 084 peaks of orth-Cu_5FeS_4, respectively. Scanning electron microscopy (SEM) images (Figures 1b, S2) show that the product predominantly forms icosahedral nanoparticles that are bound by 20 triangular facets and reveal both 5-fold and 3-fold symmetry (insets of Figures 1b,c). Transmission electron microscopy (TEM) images (Figures 1c, S3) reveal projected hexagonal shape (due to that the viewing direction is close to the 3-fold axis direction) and confirm the particle size (the distance between two opposite "edges") to be 70-180 nm. To evaluate the chemical composition of and element distribution in the nanoparticles, ultrathin sections from icosahedrons were prepared (see Supporting Information). Energy dispersive X-ray spectroscopy (EDS) elemental mapping (Figure 1d) reveals the existence of Cu, Fe and S with unevenly distributed Cu and Fe. The core is much richer in Fe than the shell while the shell contains more Cu, demonstrating a core-shell structure. Quantitative analysis based on EDS mappings (Figure S4, Table S1) shows that the Cu:Fe:S atomic ratios are close to $Cu_{48.1\pm3.9}Fe_{13.6\pm1.9}S_{38.3\pm2.7}$ and $Cu_{60.8\pm2.7}Fe_{6.1\pm1.2}S_{33.1\pm2.2}$ for the core and shell respectively, which are both non-stoichiometric Cu_5FeS_4 while the shell is Fe-deficient.

Selected area electron diffraction (SAED) patterns and high resolution TEM (HRTEM) images were further collected to investigate the crystal structure of the core-shell structure. SAED pattern (Figure S5) was collected from an icosahedron with the incident electron beam parallel to its 5-fold axis, which demonstrates the 5-fold symmetry and can be indexed to 5 SAED patterns along [110] zone axis of cubic-Cu_5FeS_4 (Figure S6) superimposed together with 4 of them rotating at 180n/5 degree (n = 1, 2, 3, 4) respectively. To collect high quality HRTEM images and distinguish the crystal structures of the core and shell, ultrathin sections of icosahedrons were selected for further TEM characterization. HRTEM image (Figure 2a) reveals high density of twin boundaries in the form of 5-fold twins, and corresponding Fast Fourier Transformed (FFT) pattern of the ultrathin section reveals 5-fold symmetry, indicating that the incident electron beam direction is parallel to the 5-fold axis of the particle. These results indicate that in principle each icosahedral nanoparticle should consist of 20 tetrahedral sub-units and therefore contain 30 twin boundaries, which is consistent with reported characterization results on cubic-structured metal icosahedral nanocrystals.[43,44] Based on this, the twin boundary density is estimated to be 1-21 x 10^{22} m^{-3}. Due to the similar crystal structure and close relation in lattice parameters between cubic- and orth-Cu_5FeS_4, sharp interface between the core and shell were not observed. Nevertheless, FFT patterns collected from single-crystalline regions of the shell (Figure 2b) and core (Figure 2c), as shown in Figure 2d and 2e respectively, are consistent with the simulated SAED patterns along [110] zone axis of cubic-Cu_5FeS_4 (Figure S6) and [210] zone axis of orth-Cu_5FeS_4 (Figure S7), respectively. HRTEM images (Figures 2b,c) give lattice spacings of 3.1 Å, which correspond to (111) and (242) planes of cubic- and orth-Cu_5FeS_4, respectively. Combined with PXRD and EDS analyses, it is concluded that the synthesized icosahedrons are non-stoichiometric orthorhombic@cubic core-shell Cu_5FeS_4 nanoparticles containing high-density twin boundaries.

2.2 Formation mechanism of Cu_5FeS_4 icosahedral nanoparticles

To understand the formation mechanism of the core-shell icosahedral nanoparticles, products synthesized after varied durations of heating (i.e. 10, 30 and 60 min) were investigated. PXRD (Figure 3a) reveals the product after 10 min of heating to be orth-Cu_5FeS_4. SEM images (Figures 3b, S8) of the as-synthesized nanoparticles, together with TEM images of ultrathin section of this sample (Figure 3c), reveal that the product is composed of nanoparticles attached by smaller particles with distinctive sizes of 70-140 and 10-20 nm, respectively. EDS elemental mapping (Figures 3d, S9) demonstrates that apart from nanoparticles with uniform distribution of Cu, Fe and S, nanoparticles with Fe-richer core and Cu-richer shell are formed as well. With increasing the heating duration to 30 min, icosahedral nanoparticles with Fe-rich core and Cu-rich shell are obtained. We speculate that S may combine with Fe more easily than Cu in our synthesis. The particle formed at the initial synthesis stage should be Fe-rich (i.e. the composition of the core); with prolonging the reaction duration, the newly formed Cu_5FeS_4 phase should be Fe-deficient, as the Fe:Cu molar ratio of the remained precursors is less than 1:5. Eventually, the core-shell nanoparticles form, with the core being Fe-rich and the shell being Cu-rich. The low Fe concentration in the shell could be one of the reasons that lead to the formation of cubic-Cu_5FeS_4 and we also notice that Fe-deficient cubic-Cu_5FeS_4 has been reported to be retained after solution synthesis.[45] The morphology evolution process of Cu_5FeS_4 icosahedral nanoparticles is demonstrated in Figure 3e. When the heating was prolonged to 60 min, with expected growth of shell and nanoparticles, the product is determined to be mixed phases of orth- and cubic-Cu_5FeS_4 with further increased fraction of the latter (Figure 3a). SEM (Figure S10) reveals the product to be icosahedral nanoparticles and a small fraction of micro-sized polyhedrons.

2.3 Characterization of Cu_5FeS_4 sintered samples

The ability to synthesize Cu_5FeS_4 core-shell icosahedral nanoparticles with controlled morphology, composition and defects in ~4 g quantities allowed the facile fabrication of sulfide pellets by spark plasma sintering (SPS) without the necessity of repeated solution preparation. Due to that non-stoichiometric, Fe-deficient Cu_5FeS_4 has higher electrical and thermal conductivity compared to nearly-stoichiometric Cu_5FeS_4,[17] the phase fraction of cubic-Cu_5FeS_4 (Cu:Fe atomic ratio of 60.8±2.7:6.1±1.2) has been controlled by adjusting SPS temperature (i.e. 748 and 773 K, denoted as 30min-748K and 30min-773K, respectively), in order to obtain optimized thermoelectric performance. PXRD (Figures 4a, S11) reveals that both pellets belong to mixed phases of orth- and cubic-Cu_5FeS_4, and with increasing SPS temperature from 748 to 773 K, the fraction of cubic-Cu_5FeS_4 decreases significantly. With higher fraction of Fe-deficient cubic-Cu_5FeS_4, 30min-748K has much higher thermal conductivity compared to 30min-773K, leading to much lower zT (Figure S12). EDS elemental mapping (Figure S13) shows that the 30min-773K pellet has more uniform distribution of Cu and Fe, indicating that SPS promoted the homogeneous distribution of both elements. This changed the composition of the shell (i.e. became less Fe-deficient) and resulted in the conversion to orth-Cu_5FeS_4 from cubic-Cu_5FeS_4.

SEM and TEM images (Figures 4b, 4c, S14, S15) reveal that the 30min-773K pellet is composed of nanoparticles that have similar particle sizes to the solution-synthesized products. Nanopores with nonuniform sizes were also observed. HRTEM image (Figure 4d) confirms the retaining of the 5-fold symmetry and high-density twin boundaries in the form of 5-fold twins. Such interfaces are expected to enhance phonon scattering, thus leading to the decrease of lattice thermal conductivity. For comparison, the products synthesized after heating for 10 and 60 min were also consolidated into pellets by SPS at 773 K (denoted as 10min-773K and 60min-773K, respectively). PXRD (Figure 4a) shows 10min-773K is pure orth-Cu_5FeS_4, while 60min-

773K is composed of orth- and cubic-Cu_5FeS_4. SEM images (Figure S16) show that 10min-773K is composed principally of fine nanoparticles while 60min-773K consists of both polyhedrons and micro-sized particles, both resembling their solution-synthesized counterparts.

2.4 Thermoelectric performance of Cu_5FeS_4 sintered samples

Figure 5 shows the thermoelectric performance of 10min-773K, 30min-773K and 60min-773K as a function of temperature. The contrast in the temperature-dependent electrical conductivity (σ) for the different pellets is striking (Figure 5a). The σ of 10min-773K (single-phase Cu_5FeS_4) increases from ~6.9×10^2 S m^{-1} at 315 K to ~7.7×10^3 S m^{-1} at 710 K. By contrast, 30min-773K, with a small fraction of more conductive Fe-deficient cubic-Cu_5FeS_4, demonstrates significantly enhanced σ (from ~5.7×10^3 S m^{-1} at 315 K to ~1.4×10^4 S m^{-1} at 710 K). With the highest fraction of cubic-Cu_5FeS_4, 60min-773K reveals the largest σ, rising from 1.3×10^4 S m^{-1} at 315 K to 2×10^4 S m^{-1} at 465 K and remaining nearly constant at higher temperature up to 685 K. Hall measurements (Table 1) give a clear correlation between the Fe deficiency (e.g. fraction of cubic-Cu_5FeS_4) and carrier concentration (n). The higher σ values ($\sigma = ne\mu$, e is the electron charge) of 60min-773K and 30min-773K are consistent with their larger n_H. The highest carrier mobility (μ_H) in 30min-773K indicates that twin boundaries have limited influence on carrier scattering. In fact, 60min-773K and 30min-773K obtain higher σ values compared to Cu_5FeS_4 bulk materials fabricated via high-temperature method (Figure S17).[12]

The p-type behavior is observed in all the three pellets, indicated by their positive Seebeck coefficient (S) within the whole temperature range (Figure 5b). S for 10min-773K increases from ~150 μV K^{-1} at 315 K to ~270 μV K^{-1} at 465 K, before decreasing to ~185 μV K^{-1} at 710 K. By contrast, S for 30min-773K and 60min-773K both keep rising with increasing the temperature yet with lower values (e.g. ~170 μV K^{-1} and ~155 μV K^{-1} at 710K, respectively). Due to much better σ values coupled with relatively high S, 30min-773K and 60min-773K

possess enhanced power factors ($S^2\sigma$), ~0.39 and ~0.45 mW m^{-1} K^{-2} at 710 K that are ~50% and ~70% larger than that of 10min-773K, respectively (Figure 5c). This clearly demonstrates that introducing the Fe-deficient cubic-Cu_5FeS_4 is very effective in optimizing electronic properties and enhancing the $S^2\sigma$ of Cu_5FeS_4.

The variation in thermal conductivity (κ) with temperature for 10min-773K and 30min-773K is very similar, maintaining very low values within the whole temperature range. κ for 30min-773K (10min-773K) decreases from ~0.43 (~0.42) W m^{-1} K^{-1} at 300 K to ~0.31 (~0.31) W m^{-1} K^{-1} at 475 (525) K, before rising to ~0.45 (~0.46) W m^{-1} K^{-1} at 710 K. These κ values are relatively low compared to other examples of Cu_5FeS_4 bulk counterparts fabricated through high-temperature synthesis and ball milling.[12, 46-47] By contrast, κ for 60min-773K reveals much higher values, decreasing from ~0.52 W m^{-1} K^{-1} at room temperature to ~0.48 W m^{-1} K^{-1} at 375-475 K before rising to ~0.68 W m^{-1} K^{-1} at 710 K.

Lattice thermal conductivity (κ_L) was estimated by subtracting κ_e (Figure S18) from κ, as shown in Figure 5e. Among all the pellets, 30min-773K possesses the lowest κ_L within the whole temperature range, decreasing from ~0.39 W m^{-1} K^{-1} at 300 K to ~0.23 W m^{-1} K^{-1} before rising to ~0.29 W m^{-1} K^{-1} at 710 K. The increasing value of κ_L at higher temperature is related to the phase transformation of Cu_5FeS_4 to high-temperature cubic phase. Two notable comparisons can be made. (1) κ_L for 30min-773K at 710 K is lower compared to that of 10min-773K, although 10min-773K has relatively smaller crystallite size. This clearly demonstrates that twin boundaries can effectively enhance acoustic phonon scattering and siginificantly reduce the κ_L; (2) κ_L for 30min-773K at 710 K is lower than that of 60min-773K although both possess twin boundaries. The increased grain size and/or the higher concentration of cubic-Cu_5FeS_4 with higher κ_L in 60min-773K should be responsible for this.

The optimized electrical properties coupled with the lower κ_L result in excellent zT values in 30min-773K, e.g. ~0.62 at 710 K that is ~51% and ~33% higher than those of single-phase

Cu_5FeS_4 pellet (10min-773K) and orthorhombic-cubic Cu_5FeS_4 pellet (60min-773K), respectively. The contrast in thermoelectric performance between the pellets underscores the importance of defect engineering, e.g. formation of high-density twin boundaries (included in icosahedral nanoparticles) and stoichiometry control (via introducing Fe-deficient cubic-Cu_5FeS_4). Notable is that zT for 30min-773K at 710 K compares very favorably with those for Cu-Fe-S compounds reported previously (Table 2). Therefore, it is achievable to synthesize twin-engineered, composition-tunable and high-performance Cu_5FeS_4 via sustainable solution methods. In principle, the present method could be extended to the synthesis of new doped Cu_5FeS_4 nanomaterials (e.g. Se doping)[47] to achieve better performance.

3. Conclusion

In summary, a colloidal solution method realizes the quick and large-scale synthesis of orthorhombic@cubic core-shell Cu_5FeS_4 icosahedral nanoparticles with high-density twin boundaries and non-stoichiometric composition. Spark plasma sintering of the nanoparticle produces nanostructured pellets. The thermal and electrical transport properties have been synergistically optimized due to inclusion of the high-density twin boundaries and a tuned fraction of Fe-deficient cubic-structured Cu_5FeS_4, resulting in an enhanced zT value of ~0.62 at 710 K. This study offers an energy-efficient route to high performing, twin-engineered, non-stoichiometric Cu_5FeS_4 thermeoelctric nanomaterials.

4. Experimental Details

Materials Synthesis. 50 mmol S powder was added to 150 ml OLA that was heated to 333 K and held for 6 h to yield a brown S-OLA solution. In parallel, 50 mmol $CuCl_2$ and 10 mmol $Fe(acac)_3$ were added to 100 ml OLA within a three-neck round-bottom flask. The solution was stirred for 6 h at room temperature under N_2 flow, heated to 453K in 5 min, and held for 10 min to get a dark brown homogeneous solution. After the $CuCl_2$-$Fe(acac)_3$-OLA solution was heated to 553 K in 3 min, the freshly prepared 150 ml S-OLA solution was rapidly poured into the

solution under N_2. The mixture was heated to 553 K again, held for either 10, 30 or 60 min and allowed to cool to 333 K under N_2. The brown-black products were washed with hexane and ethanol, and then dispersed in a mixture of hydrazine and hexane to remove coated organic ligands. The hydrazine-treated nanoparticles were collected and dried under vacuum for 3 h at 333 K. Powders were densified in a graphite die using SPS (uniaxial pressure of ~45 MPa; 773 K; 3 min).

Materials Characterization and performance evaluation. PXRD patterns were collected by a PANalytical X'pert diffractometer (Cu Kα1 radiation, λ = 1.5406 Å). The morphology of products were investigated by SEM (JEOL JSM-7800F, 5 kV). Further imaging and SAED were performed by TEM (JEOL 2100F, 200 kV and FEI Titan G2 60-300, 300 kV). Elemental mappings were collected using the FEI microscope equipped with a EDS (super-EDS) system. The Seebeck coefficient and electrical conductivity of sintered pellets were measured simultaneously using a Linseis LSR-3 instrument from 310 to 710 K. The thermal conductivity (κ) was calculated using $\kappa = DC_p\rho$, where thermal diffusivity (D) was measured using a Netzsch LFA-457 instrument from 300 to 710 K, specific heat capacity (C_p) was measured using a differential scanning calorimeter (Netzsch, 404F3), and sample density (ρ) was measured using Archimedes' method. Hall measurements were performed on a home-made apparatus under a reversible magnetic field of 1.0 T.

Supporting Information

Supporting Information is available from the Wiley Online Library or from the author.

Acknowledgements

This work was financially supported in part by the National Natural Science Foundation of China (Grant Nos. 11344010, 11404044, 51472036), the Fundamental Research Funds for the Central Universities of China (Grant Nos. 106112016CDJZR308808, 0903005203541). The work conducted at the Chongqing Institute of Green and Intelligent Technology, Chinese

Academy of Sciences is also supported by Key Research Program of Frontier Sciences, CAS (Grant No. QYZDB-SSW-SLH016) and the Project for Fundamental and Frontier Research in Chongqing (CSTC2015JCYJBX0026). JYD acknowledges the financial support from Hong Kong GRF Grant (No: B-Q55T) and PolyU (Grant Nos: G-YBFT and 1-BBAF).

Received: ((will be filled in by the editorial staff))
Revised: ((will be filled in by the editorial staff))
Published online: ((will be filled in by the editorial staff))

References

[1] J. Baxter, Z. Bian, G. Chen, D. Danielson, M. S. Dresselhaus, A. G. Fedorov, T. S. Fisher, C. W. Jones, E. Maginn, U. Kortshagen, A. Manthiram, A. Nozik, D. R. Rolison, T. Sands, L. Shi, D. Sholl, Y. Wu, *Energy Environ. Sci.* **2009**, *2*, 559.
[2] S. Chu, A. Majumdar, *Nature* **2012**, *488*, 294.
[3] G. J. Snyder, E. S. Toberer, *Nat. Mater.* **2008**, *7*, 105.
[4] G. J. Tan, L. D. Zhao, M. G. Kanatzidis, *Chem. Rev.* **2016**, *116*, 12123.
[5] M. S. Dresselhaus, G. Chen, M. Y. Tang, R. G. Yang, H. Lee, D. Z. Wang, Z. F. Ren, J. P. Fleurial, P. Gogna, *Adv. Mater.* **2007**, *19*, 1043.
[6] Y. Lan, A. J. Minnich, G. Chen, Z. Ren, *Adv. Funct. Mater.* **2010**, *20,* 357.
[7] J. Yang, L. Xi, W. Qiu, L. Wu, X. Shi, L. Chen, J. Yang, W. Zhang, C. Uher, D. J. Singh, *NPJ Comput. Mater* **2016**, *2*, 15015.
[8] G. Han, Z.-G. Chen, J. Drennan, J. Zou, *Small* **2014**, 10, 2747.
[9] X. Lu, D. T. Morelli, Y. Xia, F. Zhou, V. Ozolins, H. Chi, X. Y. Zhou, C. Uher, *Adv. Energy Mater.* **2013**, *3*, 342.
[10] Y. He, T. Day, T. S. Zhang, H. L. Liu, X. Shi, L. D. Chen, G. J. Snyder, *Adv. Mater.* **2014**, *26*, 3974.
[11] H. Y. Xie, X. L. Su, G. Zheng, T. Zhu, K. Yin, Y. G. Yan, C. Uher, M. G. Kanatzidis, X. F. Tang, *Adv. Energy Mater.* **2017**, *7*, 1601299.
[12] P. F. Qiu, T. S. Zhang, Y. T. Qiu, X. Shi, L. D. Chen, *Energy Environ. Sci.* 2014, *7*, 4000.
[13] D. Berthebaud, O.I. Lebedev, A. Maignan, *J. Materiomics* **2015**, *1*, 68.
[14] N. Tsujii and T. Mori, *Appl. Phys. Express* **2013**, *6*, 043001.
[15] R. Ang, A. U. Khan, N. Tsujii, K. Takai, R. Nakamura, T. Mori, *Ang et al. Angew. Chem. Int. Ed.* **2015**, *54*, 12909.
[16] N. Tsujii, T. Mori, Y. Isoda, *J. Elec. Mater.* **2014**, *43*, 2371.
[17] A. J. Zhang, X. C. Shen, Z. Zhang, X. Lu, W. Yao, J. Y. Dai, D. D. Xie, L. J. Guo, G. Y. Wang, X. Y. Zhou, *J. Mater. Chem. C* **2017**, *5*, 301.
[18] Z. Li, C. Xiao, H. Zhu, Y. Xie, *J. Am. Chem. Soc.* **2016**, *138*, 14810.
[19] Y. F. Liu, M. H. Zhou, J. He, *Scripta Mater.* **2016**, *111*, 39.
[20] L. H. Wang, X. D. Han, P. Liu, Y. H. Yue, Z. Zhang, E. Ma, *Phys. Rev. Lett.* **2010**, *105*, 4.
[21] K. Biswas, J. Q. He, I. D. Blum, C. I. Wu, T. P. Hogan, D. N. Seidman, V. P. Dravid, M. G. Kanatzidis, *Nature* **2012**, *489*, 414.
[22] L. P. Hu, T. J. Zhu, X. H. Liu, X. B. Zhao, *Adv. Funct. Mater.* **2014**, 24, 5211.
[23] G. Y. Jiang, J. He, T. J. Zhu, C. G. Fu, X. H. Liu, L. P. Hu, X. B. Zhao, *Adv. Funct.*

Mater. **2014**, *24*, 3776.
[24] W. Li, L. L. Zheng, B. H. Ge, S. Q. Lin, X. Y. Zhang, Z. W. Chen, Y. J. Chang, Y. Z. Pei, *Adv. Mater.* **2017**, *29*, 8.
[25] K. Biswas, J. He, Q. Zhang, G. Wang, C. Uher, V. P. Dravid, M. G. Kanatzidis, *Nat. Chem.* **2011**, *3*, 160.
[26] Q. Zhang, Y. C. Lan, S. L. Yang, F. Cao, M. L. Yao, C. Opeil, D. Broido, G. Chen, Z. F. Ren, *Nano Energy* **2013**, *2*, 1121.
[27] Y.-X. Chen, Z.-H. Ge, M. Yin, D. Feng, X.-Q. Huang, W. Zhao, J. He, *Adv. Funct. Mater.* **2016**, *26*, 6836.
[28] J. P. Heremans, V. Jovovic, E. S. Toberer, A. Saramat, K. Kurosaki, A. Charoenphakdee, S. Yamanaka, G. J. Snyder, *Science* **2008**, *321*, 554.
[29] L.-D. Zhao, G. Tan, S. Hao, J. He, Y. Pei, H. Chi, H. Wang, S. Gong, H. Xu, V. P. Dravid, C. Uher, G. J. Snyder, C. Wolverton, M. G. Kanatzidis, *Science* **2015**, *351*, 141.
[30] K. Peng, X. Lu, H. Zhan, S. Hui, X. Tang, G. Wang, J. Dai, C. Uher, G. Wang, X. Zhou, *Energy Environ. Sci.* **2016**, *9*, 454.
[31] Y. Pei, X. Shi, A. LaLonde, H. Wang, L. Chen, G. J. Snyder, *Nature* **2011**, *473*, 66.
[32] G. J. Tan, F. Y. Shi, S. Q. Hao, H. Chi, L. D. Zhao, C. Uher, C. Wolverton, V. P. Dravid, M. G. Kanatzidis, *J. Am. Chem. Soc.* **2015**, *137*, 5100.
[33] Q. Zhang, B. L. Liao, Y. C. Lan, K. Lukas, W. S. Liu, K. Esfarjani, C. Opeil, D. Broido, G. Chen, Z. F. Ren, *Proc. Natl. Acad. Sci.* **2013**, *110*, 13261.
[34] T.-R. Wei, G. Tan, X. Zhang, C.-F. Wu, J.-F. Li, V. P. Dravid, G. J. Snyder, M. G. Kanatzidis, *J. Am. Chem. Soc.* **2016**, *138*, 8875.
[35] Y. Liu, L. D. Zhao, Y. C. Liu, J. L. Lan, W. Xu, F. Li, B. P. Zhang, D. Berardan, N. Dragoe, Y. H. Lin, C. W. Nan, J. F. Li, H. M. Zhu, *J. Am. Chem. Soc.* **2011**, *133*, 20112.
[36] J. Mao, Y. N. Wang, H. S. Kim, Z. H. Liu, U. Saparamadu, F. Tian, K. Dahal, J. Y. Sun, S. Chen, W. S. Liu, Z. F. Ren, *Nano Energy* **2015**, *17*, 279.
[37] Y. Yu, D. S. He, S. Y. Zhang, O. Cojocaru-Miredin, T. Schwarz, A. Stoffers, X. Y. Wang, S. Q. Zheng, B. Zhu, C. Scheu, D. Wu, J. Q. He, M. Wuttig, Z. Y. Huang, F. Q. Zu, *Nano Energy* **2017**, *37*, 203.
[38] H. Fang, Z. Luo, H. Yang, Y. Wu, *Nano Lett.* **2014**, *14*, 1153.
[39] M. Ibáñez, R. J. Korkosz, Z. S. Luo, P. Riba, D. Cadavid, S. Ortega, A. Cabot, M. G. Kanatzidis, *J. Am. Chem. Soc.* **2015**, *137*, 4046.
[40] F. J. Fan, Y. X. Wang, X. J. Liu, L. Wu, S. H. Yu, *Adv. Mater.* **2012**, *24*, 6158.
[41] G. Han, S. R. Popuri, H. F. Greer, L. F. Llin, J. W. G. Bos, W. Z. Zhou, D. J. Paul, H. Ménard, A. R. Knox, A. Montecucco, J. Siviter, E. A. Man, W.-g. Li, M. C. Paul, M. Gao, T. Sweet, R. Freer, F. Azough, H. Baig, T. K. Mallick, D. H. Gregory, *Adv. Energy Mater.* **2017**, *7*, 1602328.
[42] R. J. Mehta, Y. Zhang, C. Karthik, B. Singh, R. W. Siegel, T. Borca-Tasciuc, G. Ramanath, *Nat. Mater.* **2012**, *11*, 233.
[43] J. B. Wu, L. Qi, H. J. You, A. Gross, J. Li, H. Yang, *J. Am. Chem. Soc.* **2012**, *134*, 11880.
[44] J. Xu, S. Y. Li, J. Weng, X. F. Wang, Z. M. Zhou, K. Yang, M. Litt, X. Chen, Q. Cui, M. Y. Cao, Q. Q. Zhang, *Adv. Funct. Mater.* **2008**, *18*, 277.
[45] A. M. Wiltrout, N. J. Freymeyer, T. Machani, D. P. Rossi, K. E. Plass, *J. Mater. Chem.* **2011**, *21*, 19286.
[46] G. Guelou, A. V. Powell, P. Vaqueiro, *J. Mater. Chem. C* **2015**, *3*, 10624.
[47] V. P. Kumar, T. Barbier, P. Lemoine, B. Raveau, V. Nassif, E. Guilmeau, *Dalton Trans.* **2017**, *46*, 2174.
[48] H. Y. Xie, X. L. Su, G. Zheng, Y. G. Yan, W. Liu, H. Tang, M. G. Kanatzidis, C. Uher, X. F. Tang, *J. Phys. Chem. C* **2016**, *120*, 27895.
[49] D. X. Liang, R. S. Ma, S. H. Jiao, G. S. Pang, S. H. Feng, *Nanoscale* **2012**, 4, 6265.

[50] J. H. Li, Q. Tan, J. F. Li, *J. Alloy. Compd.* **2013**, *551*, 143.
[51] T. Barbier, D. Berthebaud, R. Fresard, O. I. Lebedev, E. Guilmeau, V. Eyert, A. Maignan, *Inorg. Chem. Front.* **2017**, *4*, 424.
[52] V. Pavan Kumar, T. Barbier, V. Caignaert, B. Raveau, R. Daou, B. Malaman, G. L. Caër, P. Lemoine, E. Guilmeau, *J. Phys. Chem. C* **2017**, *121*, 16454.

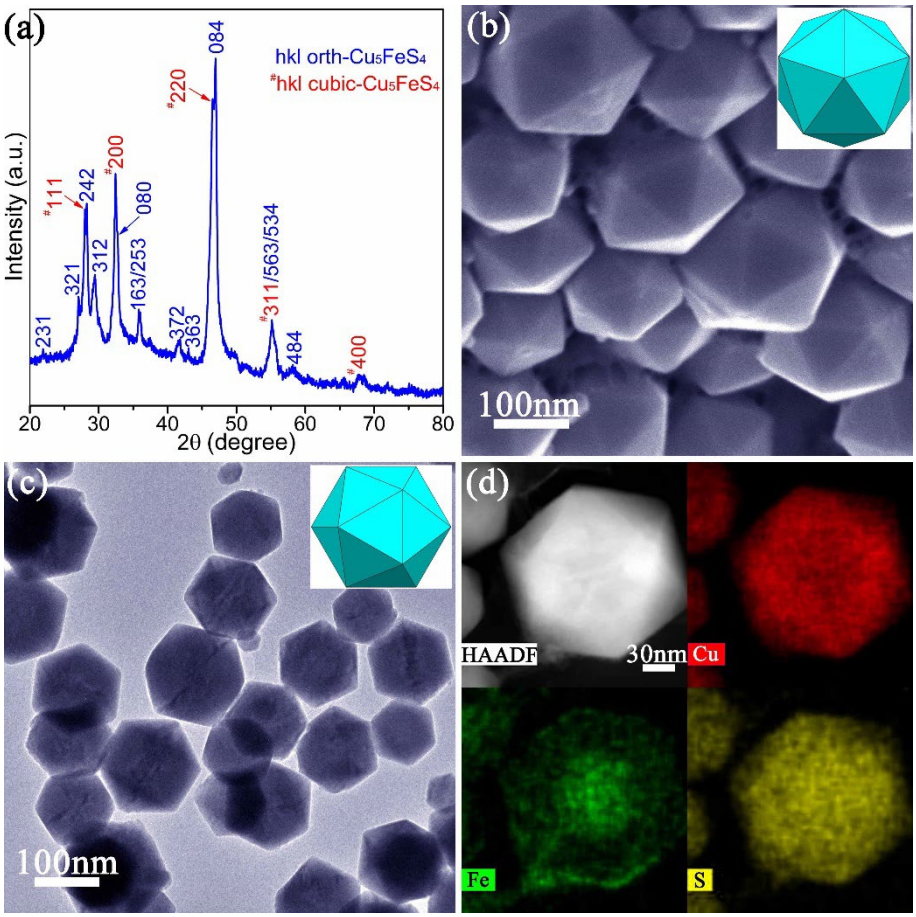

Figure 1. Characterization of Cu_5FeS_4 nanoparticles synthesized after 30 min of heating: (a) PXRD pattern, (b) SEM image and (c) TEM image of the as-synthesized nanoparticles; (d) EDS mapping of ultrathin sections prepared from the nanoparticles. Insets in (b) and (c) are models of an icosahedron viewed along its 5-fold and 3-fold axes, respectively. The four panels in (d) are high angle annular dark field (HAADF) image, elemental mappings for Cu (red), Fe (green) and S (yellow).

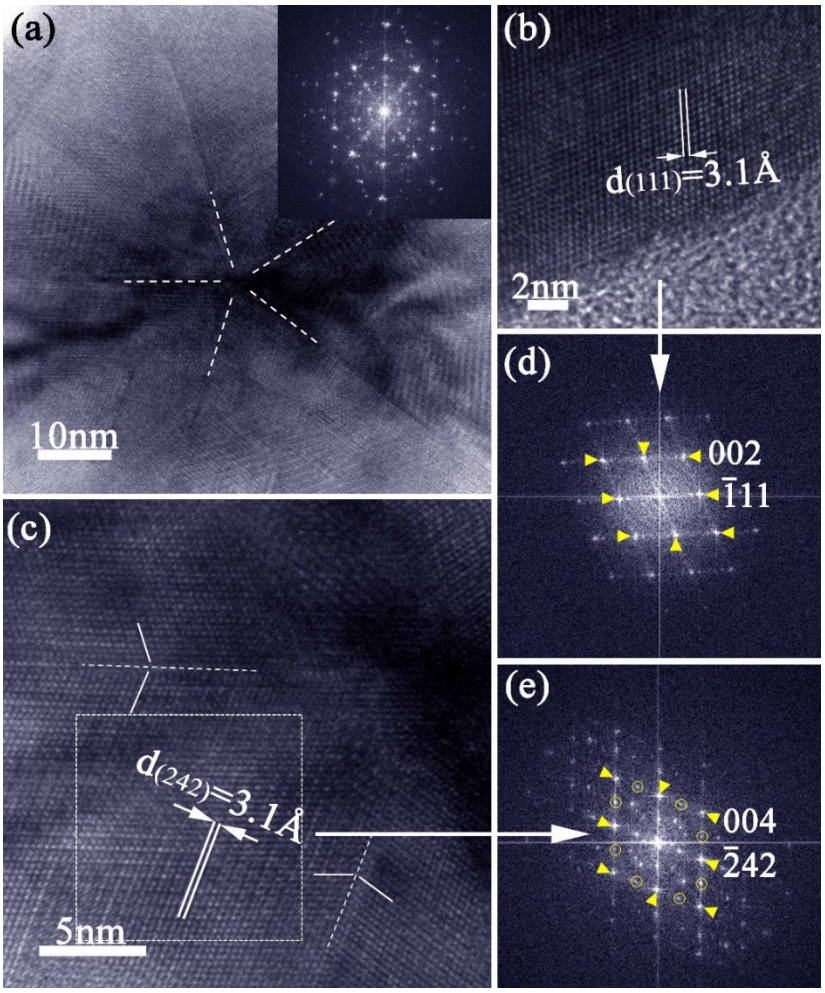

Figure 2. TEM characterization of an ultrathin section prepared from a Cu_5FeS_4 core-shell nanoparticle: (a-c) HRTEM images collected from a particle, its shell and core, respectively; inset of (a), (d), (e) FFT patterns collected from the nanoparticle, its shell and core, respectively.

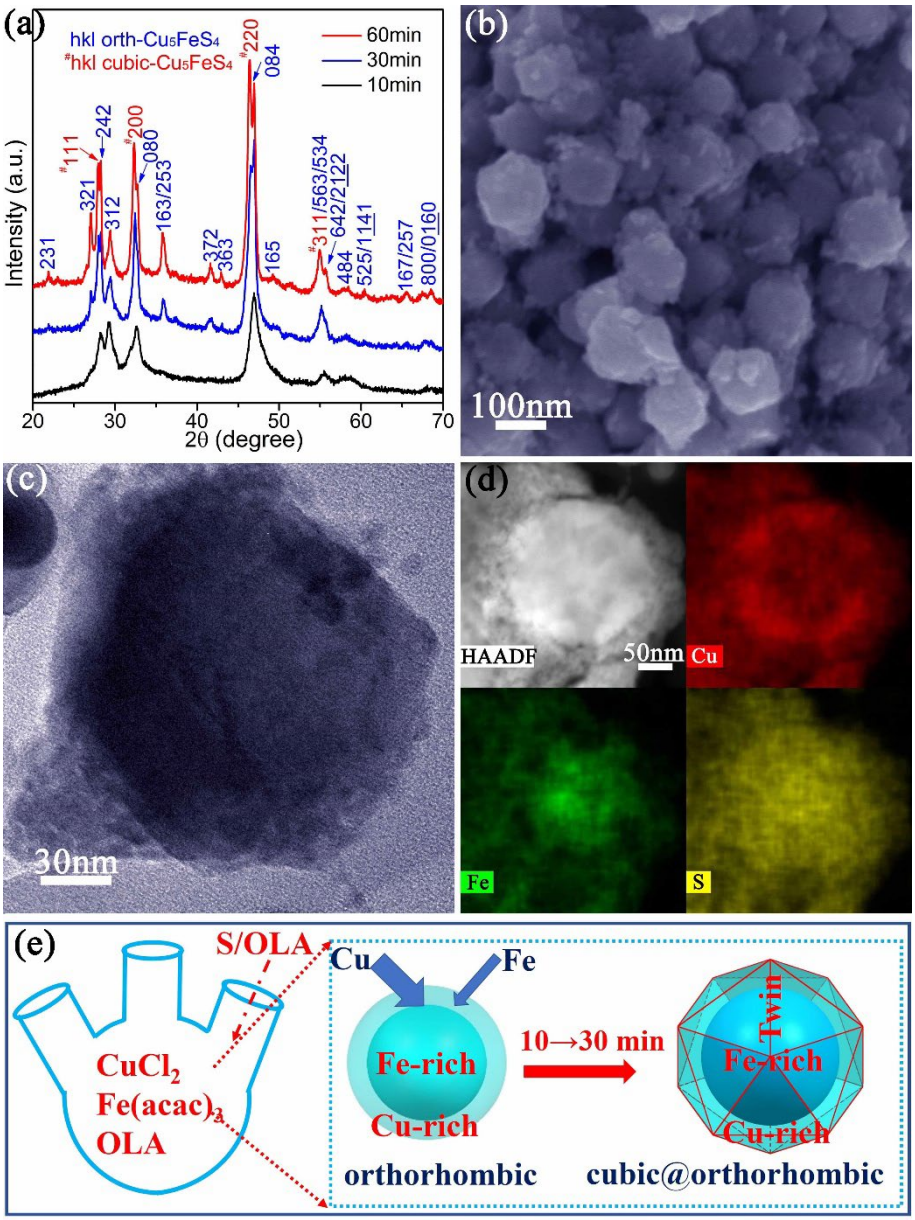

Figure 3. Characterization of Cu_5FeS_4 nanoparticles synthesized after various heating durations: (a) PXRD patterns, (b) SEM image of the nanoparticles (10 min product), (c) and (d) TEM image and EDS mapping of ultrathin sections prepared from the nanoparticles (10 min product), (e) schematics showing the formation process of Cu_5FeS_4 icosahedral core-shell nanoparticles. The four panels in (d) are HAADF image, elemental mappings for Cu (red), Fe (green) and S (yellow).

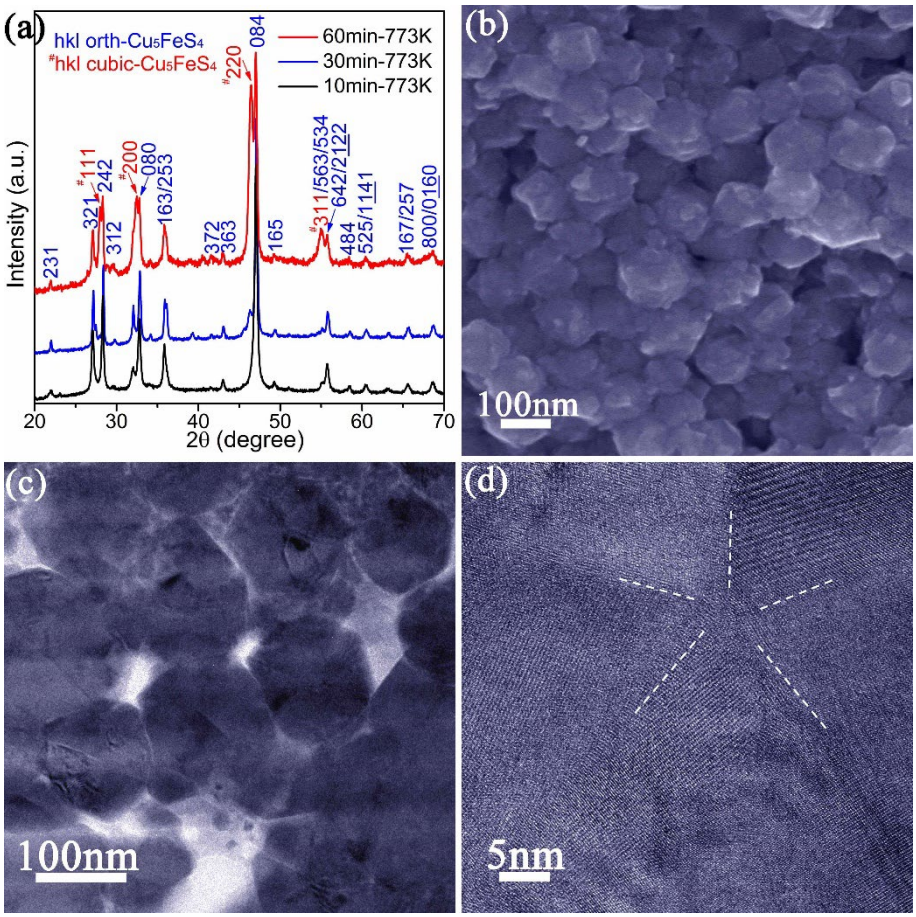

Figure 4. Characterization of Cu_5FeS_4 pellets consolidated from products synthesized after various heating durations: (a) PXRD patterns, (b) SEM image of 30min-773K pellet, (c), (d) TEM and HRTEM images of ultrathin sections prepared from 30min-773K pellet.

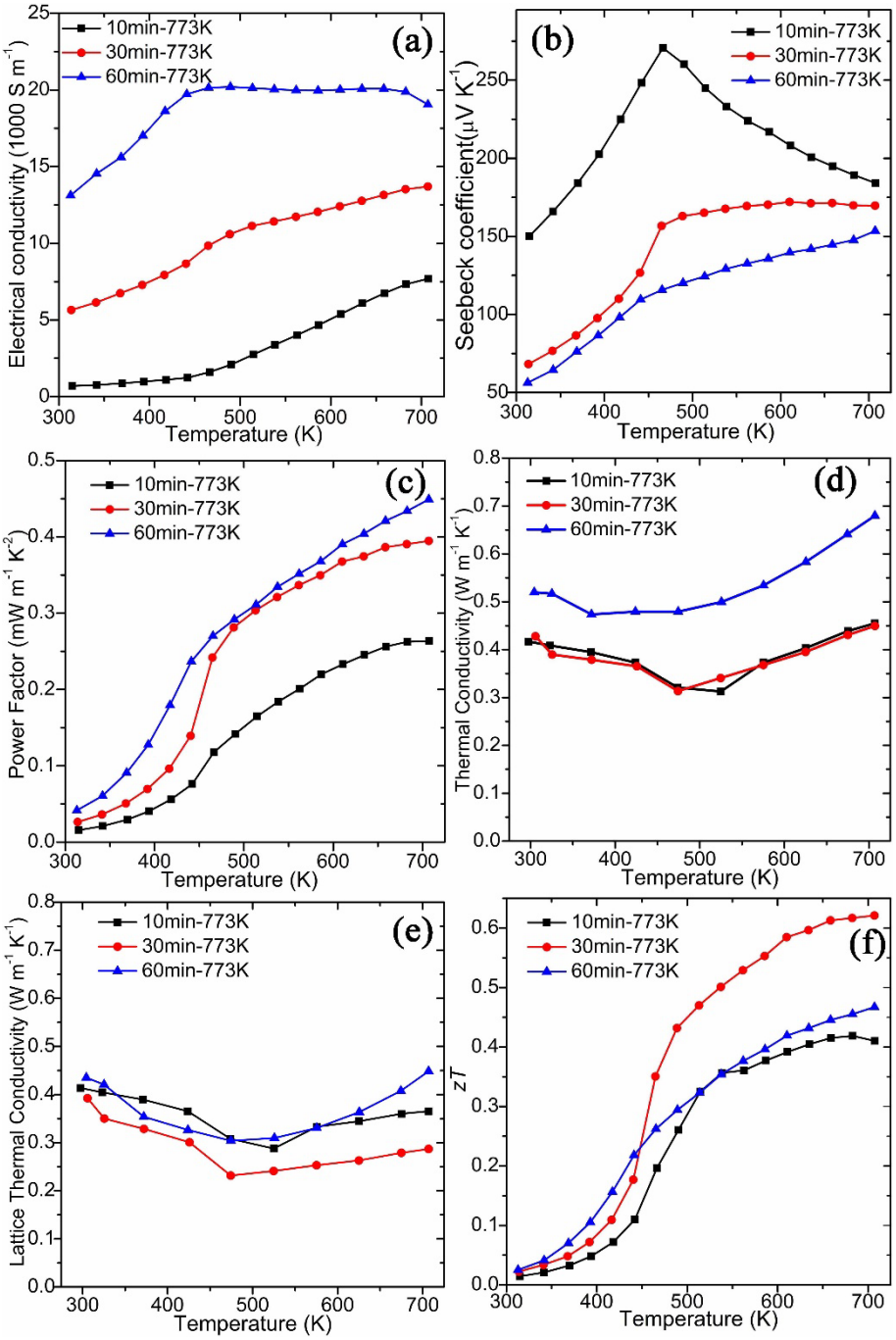

Figure 5. Thermoelectric properties of Cu_5FeS_4 pellets 10min-773K, 30min-773K and 60min-773K: (a) σ, (b) S, (c) $S^2\sigma$, (d) κ, (e) κ_L and (f) zT as a function of temperature.

Table 1. A summary of electronic properties, room temperature Hall carrier concentration (n_H) and mobility (μ_H) and lattice thermal conductivity (κ_L) of the pellets.

Pellet	σ_{310K} [S m^{-1}]	S_{310K} [μV K^{-1}]	n_H [10^{20} cm^{-3}]	μ_H [cm^2 V^{-1} s^{-1}]	$(\kappa_L)_{300K}$ [W m^{-1} K^{-1}]
10min-773K	6.9×10^2	150	1.8	0.24	0.41
30min-773K	5.6×10^3	68	6.5	0.55	0.39
60min-773K	1.3×10^4	56	41	0.20	0.44

Table 2. A summary of thermoelectric properties of Cu-Fe-S compounds

Materials	T[a)] [K]	zT[b)]	$S^2\sigma$[b)] [mW m^{-1} K^{-2}]	κ[b)] [W m^{-1} K^{-1}]	Synthesis method	References
Cu_5FeS_4	710	0.62	0.39	0.45	colloidal synthesis+SPS	this work
Cu_5FeS_4	700	~0.38	~0.25	~0.485	melting+annealing+SPS	[12]
$Cu_{5.04}Fe_{0.96}S_4$	700	0.52	0.35	~0.49	melting+annealing+SPS	[12]
$Cu_5Fe_{0.95}Mn_{0.05}S_4$	543	0.55	0.34	0.33	ball milling+hot pressing	[46]
Cu_5FeS_4	690	0.56	0.4	0.47	colloidal synthesis+SPS	[17]
$Cu_5FeS_{3.8}Se_{0.2}$	540	0.5	0.43	0.47	ball milling+SPS	[47]
$Cu_{0.92}Zn_{0.08}FeS_2$	630	0.26	~0.84	2.08	melting+annealing+SPS	[11]
$CuFe_{0.96}In_{0.04}S_2$	630	0.17	~0.46	~1.66	melting+annealing+PAS[c)]	[48]
$CuFeS_2$	500	0.264	0.23	0.439	solution synthesis+hot pressing	[49]
$CuFeS_{1.8}$	573	0.21	0.656	~1.85	mechanical alloying+SPS	[50]
$CuFe_2S_3$	673	0.13	~0.49	2.58	melting+annealing+SPS	[51]
$Cu_{8.5}Fe_{2.5}Sn_2S_{12}$	630	0.35	~0.52	~0.93	ball milling+SPS	[52]
$Zn_{0:03}Cu_{0:97}FeS_2$	400	0.07	1.1	~6	melting+annealing+SPS	[14]
$Cu_{0.94}Co_{0.06}FeS_2$	675	0.22	0.55	~1.6	melting+annealing+SPS	[13]

[a)] The temperature at which maximum zT was achieved; [b)] zT, $S^2\sigma$ and κ at T; [c)] plasma activated sintering.